Alignment and signed-intensity anomalies in WMAP data

P. Vielva[1], Y. Wiaux[2], E. Martínez-González[1], P. Vandergheynst[2]

[1] *Instituto de Física de Cantabria (CSIC - UC), 39005 Santander, Spain*
  E-mails : vielva@ifca.unican.es, martinez@ifca.unican.es
[2] *Signal Processing Institute, Ecole Polytechnique Fédérale de Lausanne (EPFL), CH-1015 Lausanne, Switzerland*
  E-mails : yves.wiaux@epfl.ch, pierre.vandergheynst@epfl.ch

1 February 2008

ABSTRACT
Significant alignment and signed-intensity anomalies of local features of the cosmic microwave background (CMB) are detected on the three-year WMAP data, through a decomposition of the signal with steerable wavelets on the sphere. In addition to identifying local features of a signal at specific scales, steerable wavelets allow one to determine their local orientation and signed-intensity. Firstly, an alignment analysis identifies two mean preferred planes in the sky, both with normal axes close to the CMB dipole axis. The first plane is defined by the directions toward which local CMB features are anomalously aligned. A mean preferred axis is also identified in this plane, located very close to the ecliptic poles axis. The second plane is defined by the directions anomalously avoided by local CMB features. This alignment anomaly provides further insight on recent results (Wiaux et al. 2006a). Secondly, a signed-intensity analysis identifies three mean preferred directions in the southern galactic hemisphere with anomalously high or low temperature of local CMB features: a cold spot essentially identified with a known cold spot (Vielva et al. 2004), a second cold spot lying very close to the southern end of the CMB dipole axis, and a hot spot lying close to the southern end of the ecliptic poles axis. In both analyses, the anomalies are observed at wavelet scales corresponding to angular sizes around $10°$ on the celestial sphere, with global significance levels around 1%. Further investigation reveals that the alignment and signed-intensity anomalies are only very partially related. Instrumental noise, foreground emissions, as well as some form of other systematics, are strongly rejected as possible origins of the detections. An explanation might still be envisaged in terms of a global violation of the isotropy of the Universe, inducing an intrinsic statistical anisotropy of the CMB.

Key words: methods: data analysis, techniques: image processing, cosmology: observations, cosmic microwave background

1 INTRODUCTION

In the light of the results obtained from the analysis of several recent high-precision data sets, a wide consensus was reached in the cosmology community on a concordance model for a flat ΛCDM Universe with a primordial phase of inflation. In this framework, the Universe is flat and filled in with cold dark matter (CDM) and dark energy in the form of a cosmological constant (Λ), in addition to the standard baryonic and electromagnetic components. The cosmological principle assumption states that the Universe is globally homogeneous and isotropic. The large scale structure and the cosmic microwave background (CMB) radiation find their origin in Gaussian quantum energy density fluctuations developed around the homogeneous and isotropic background,

as predicted by the standard inflationary scenario taking place in the primordial Universe.

The CMB data, and specifically the data provided by the NASA Wilkinson Microwave Anisotropy Probe (WMAP) satellite experiment, have played a leading role in defining this concordance model (Bennett et al. 2003a; Spergel et al. 2003; Hinshaw et al. 2007; Spergel et al. 2007). However anomalies have been reported. They naturally question the basic hypotheses on which the model relies, in particular the Gaussianity (assumed by the standard inflationary scenario) and statistical isotropy (postulated by the cosmological principle) of the statistical distribution from which the CMB temperature fluctuations arise in the primordial Universe.

Departures from Gaussianity of the one-year and three-year WMAP data have been reported in terms of vari-

ous statistics. Firstly, non-Gaussianity was notably detected through the use of a genus-based statistic (Park 2004). Secondly, wavelet analyses have also reported non-Gaussian deviations. An excess in the kurtosis of the wavelet coefficients of the axisymmetric Mexican hat wavelet on the sphere was found at wavelet scales corresponding to angular sizes on the celestial sphere around $10°$ (Vielva et al. 2004). This deviation is located in the southern galactic hemisphere, where a very cold spot was identified at $(\theta, \varphi) = (147°, 209°)$, with $\theta \in [0, \pi]$ and $\varphi \in [0, 2\pi)$ respectively standing for the co-latitude and longitude in galactic spherical coordinates. This detection was confirmed with various wavelets and various statistics (Mukherjee & Wang 2004; Cruz et al. 2005; Cayón et al. 2005; McEwen et al. 2005; Cruz et al. 2006, 2007; McEwen et al. 2006). Notice that the cold spot identified not only bears non-Gaussianity, but also represents a departure from statistical isotropy, in terms of a North-South asymmetry in galactic coordinates.

Departures from statistical isotropy of the one-year and three-year WMAP data have also been reported in terms of various statistics.

Firstly, a North-South asymmetry in ecliptic coordinates has been detected through the use of N-point correlation functions (Eriksen et al. 2004a, 2005), Minkowski functionals (Eriksen et al. 2004b), local power spectra (Hansen et al. 2004b; Donoghue & Donoghue 2005), local bispectra (Land & Magueijo 2005a), and local curvature (Hansen et al. 2004a). The asymmetry is maximum in a coordinate system with the North pole lying at $(\theta, \varphi) = (80°, 57°)$, close to the northern end of the ecliptic poles axis at $(\theta, \varphi) = (60°, 96°)$. This North-South asymmetry was confirmed through the application of a pair angular-separation histogram method (Bernui et al. 2006, 2007). More recently, it was again observed through the search for a best-fit dipolar modulation of the three-year WMAP data (Spergel et al. 2007; Eriksen et al. 2007). The corresponding dipolar axis has a northern end at $(\theta, \varphi) = (63°, 45°)$.

Secondly, an anomalous alignment of the lowest multipoles of the WMAP data was reported, especially at $\ell = 2, 3$ (de Oliveira-Costa et al. 2004; Schwarz et al. 2004; Copi et al. 2004; Katz & Weeks 2004; Bielewicz et al. 2005), but also up to $\ell = 5$ (Land & Magueijo 2005b; Abramo et al. 2006), and for $\ell = 6, 7$ (Freeman et al. 2006). This alignment highlights the so-called axis of evil, with northern end at $(\theta, \varphi) = (30°, 260°)$, very close to the CMB dipole axis, with northern end at $(\theta, \varphi) = (42°, 264°)$. Very recently, a new statistic to analyze the alignment of multipoles that is robust against treatments of the galactic plane was proposed (Land & Magueijo 2006). The corresponding analysis highlights a weaker detection for these alignments.

The large scale fluctuations of the CMB were also pointed out to fit with the expected pattern of an anisotropic Bianchi VII$_h$ Universe (Jaffe et al. 2006a,c; Bridges et al. 2006), although the cosmological parameters derived from this hypothesis are ruled-out (Jaffe et al. 2006b; Bridges et al. 2006). Notice on the contrary that bipolar power spectra analyses are consistent with no violation of the statistical isotropy of the Universe (Hajian & Souradeep 2005, 2003; Hajian et al. 2005).

Finally, in a previous work, we detected a very significant deviation from statistical isotropy of the one-year WMAP data through the use of a novel alignment analysis, based on the decomposition of the WMAP data with steerable wavelets on the sphere (Wiaux et al. 2006a). This alignment analysis probes the anomalous alignment of local CMB features toward specific directions on the celestial sphere. At wavelet scales corresponding to angular sizes around $10°$, an anomalous alignment is observed toward a mean preferred plane in the sky, whose normal axis, with a northern end at $(\theta, \varphi) = (34°, 331°)$, is close to the CMB dipole axis and close to the axis of evil. In addition, a prominent cluster of directions toward which local features are aligned identifies a mean preferred axis in this plane, with a northern end at $(\theta, \varphi) = (71°, 91°)$, very close to the ecliptic poles axis. The detection of this alignment anomaly actually synthesized the previously reported statistical anisotropy results by highlighting both the ecliptic poles axis and the CMB dipole axis as preferred axes in the sky. But further analyses were still required to establish their origin.

The aim of this paper is to probe further the statistical isotropy of the CMB through two different analyses. Firstly, we reproduce, on the three-year WMAP data, the previously discussed alignment analysis of the local CMB features originally performed on the one-year WMAP data. Secondly, we propose a signed-intensity analysis of the local CMB features, based on the same steerable wavelet decomposition of the three-year WMAP data. This signed-intensity analysis probes the anomalously high or low temperature of local CMB features. The paper is organized as follows. In Section 2, we discuss the overall methodologies defined for the subsequent analyses. In Section 3, we present the results of analysis of the three-year WMAP data. In Section 4, we investigate possible origins for the anomalies observed. We finally conclude in Section 5.

2   METHODOLOGIES

In this section, we firstly recall the notion of wavelet steerability and present the particular steerable wavelet on the sphere used in the subsequent analysis. Secondly, we discuss how to differentiate between statistical anisotropy and non-Gaussianity detections through the analysis of the CMB data with simulations produced following the concordance model. We finally recall the procedure for the alignment analysis, and define the new procedure for the signed-intensity analysis, both intended to probe the statistical isotropy of the CMB data.

2.1   Steerable wavelets

A practical approach to the formalism of continuous wavelets on the sphere (*i.e.* the unit sphere S^2), and the corresponding notion of steerable wavelets were recently introduced (Wiaux et al. 2005). Let us primarily fix some notations. We consider a three-dimensional Cartesian coordinate system $(o, o\hat{x}, o\hat{y}, o\hat{z})$ centered on the sphere, and where the direction $o\hat{z}$ identifies the North pole. Any point ω on the sphere is identified by its corresponding spherical coordinates (θ, φ), where $\theta \in [0, \pi]$ stands for the co-latitude, and $\varphi \in [0, 2\pi)$ for the longitude. Any filter invariant under rotation around itself is said to be axisymmetric. By definition, any non-axisymmetric, or directional, filter is steerable if a rotation by $\chi \in [0, 2\pi)$ around itself may be expressed

in terms of a finite linear combination of non-rotated basis filters. In this work, we consider the second Gaussian derivative wavelet (2GD), $\Psi^{\partial_{\hat{x}}^2 (gau)}$, which is obtained by a stereographic projection of the second derivative in direction $\hat{x}$ of a Gaussian in the tangent plane at the North pole. The filter obtained is a steerable wavelet on the sphere which may be rotated in terms of three basis filters: the second derivative in the direction $\hat{x}$ itself, $\Psi^{\partial_{\hat{x}}^2 (gau)}$, the second derivative in the direction $\hat{y}$, $\Psi^{\partial_{\hat{y}}^2 (gau)}$, and the cross-derivative, $\Psi^{\partial_{\hat{x}} \partial_{\hat{y}} (gau)}$ (Wiaux et al. 2005). These basis filters dilated at any scale $a \in \mathbb{R}_+^*$ read:

$$\Psi_a^{\partial_{\hat{x}}^2 (gau)} (\theta, \varphi) \quad = \quad f_a (\theta) \left[1 - \frac{4}{a^2} \tan^2 \frac{\theta}{2} \cos^2 \varphi \right] \qquad (1)$$

$$\Psi_a^{\partial_{\hat{y}}^2 (gau)} (\theta, \varphi) \quad = \quad f_a (\theta) \left[1 - \frac{4}{a^2} \tan^2 \frac{\theta}{2} \sin^2 \varphi \right] \qquad (2)$$

$$\Psi_a^{\partial_{\hat{x}} \partial_{\hat{y}} (gau)} (\theta, \varphi) \quad = \quad f_a (\theta) \left[- \frac{2}{a^2} \tan^2 \frac{\theta}{2} \sin 2\varphi \right], \qquad (3)$$

where $f_a(\theta) = a^{-1} \sqrt{4/3\pi} (1 + \tan^2(\theta/2)) e^{-2\tan^2(\theta/2)/a^2}$. The value of the scale a identifies with the dispersion of the Gaussian in units of $2 \tan(\theta/2)$. The angular size of the 2GD is defined as twice the half-width of the wavelet, where the half-width is defined by $\theta_{hw} = 2 \arctan(a/2)$, which is closely approximated by a at small scales.

The analysis of a signal F with a given wavelet Ψ simply defines a set of wavelet coefficients $W_\Psi^F (\omega_0, \chi, a)$, which result from the directional correlation between F and the wavelet dilated at any scale a, Ψ_a. In other words these wavelet coefficients are defined by the scalar product between the signal and the wavelet dilated at scale a, rotated around itself by χ, and translated at any point ω_0 on the sphere, also denoted $\Psi_{\omega_0, \chi, a}$:

$$W_\Psi^F (\omega_0, \chi, a) = \langle \Psi_{\omega_0, \chi, a} | F \rangle = \int_{S^2} d\Omega \Psi_{\omega_0, \chi, a}^* (\omega) F(\omega). \quad (4)$$

The * denotes complex conjugation. The wavelet coefficients of a signal therefore characterize the signal at each scale a, orientation χ, and position ω_0. By linearity of the operation defining wavelet coefficients from the wavelet, the relation of steerability of the wavelet is automatically transferred to the wavelet coefficients. The specific steerability relation for the wavelet coefficients of a signal F with the 2GD reads:

$$\begin{aligned} W_{\Psi^{\partial_{\hat{x}}^2}}^F (\omega_0, \chi, a) \quad = \quad & W_{\Psi^{\partial_{\hat{x}}^2}}^F (\omega_0, a) \cos^2 \chi \\ & + W_{\Psi^{\partial_{\hat{y}}^2}}^F (\omega_0, a) \sin^2 \chi \\ & + W_{\Psi^{\partial_{\hat{x}} \partial_{\hat{y}}}}^F (\omega_0, a) \sin 2\chi, \end{aligned} \qquad (5)$$

where $W_{\Psi^{\partial_{\hat{x}}^2}}^F (\omega_0, a)$, $W_{\Psi^{\partial_{\hat{y}}^2}}^F (\omega_0, a)$, and $W_{\Psi^{\partial_{\hat{x}} \partial_{\hat{y}}}}^F (\omega_0, a)$ are the wavelet coefficients respectively obtained from the standard correlation (*i.e.* $\chi = 0$) of the signal with $\Psi_a^{\partial_{\hat{x}}^2 (gau)}$, $\Psi_a^{\partial_{\hat{y}}^2 (gau)}$ and $\Psi_a^{\partial_{\hat{x}} \partial_{\hat{y}} (gau)}$.

At each scale a and at each position ω_0, one is typically interested in one or a few of the infinite number of wavelet coefficients associated with the infinite number of orientations χ (Wiaux et al. 2005; McEwen et al. 2007). Selecting the orientation $\chi_0(\omega_0, a)$ that maximizes the absolute value of the wavelet coefficient, corresponds to selecting the local orientation at which the wavelet best matches the local feature of the signal. Notice that, as the 2GD is invariant under rotation around itself by π, orientations may arbitrarily be constrained in a range of length π. As $\Psi_a^{\partial_{\hat{x}}^2 (gau)}$ oscillates in the tangent direction $\hat{x}$, it actually detects features aligned along the tangent direction $\hat{y}$. Hence, the local orientation of the feature itself, $D^F(\omega_0, a)$, is defined in terms of $\chi_0 = \chi_0(\omega_0, a)$ as:

$$\frac{\pi}{2} \leqslant D^F(\omega_0, a) = \chi_0 + \frac{\pi}{2} < \frac{3\pi}{2}. \qquad (6)$$

For the particular case of the 2GD, the steerability relation (5) enables to compute the orientation χ_0 from the wavelet coefficients obtained from the basis filters as:

$$\tan 2\chi_0 = \frac{2 W_{\Psi^{\partial_{\hat{x}} \partial_{\hat{y}}}}^F (\omega_0, a)}{W_{\Psi^{\partial_{\hat{x}}^2}}^F (\omega_0, a) - W_{\Psi^{\partial_{\hat{y}}^2}}^F (\omega_0, a)}. \qquad (7)$$

The wavelet coefficient itself at scale a, position ω_0, and in direction χ_0, defines to so-called signed-intensity of the local feature:

$$I^F(\omega_0, a) = W_{\Psi^{\partial_{\hat{x}}^2}}^F (\omega_0, \chi_0, a). \qquad (8)$$

Analyzing signals with steerable wavelets is interesting in several respects. Firstly, the wavelet decomposition enables one to identify the scales a of the physical processes which define the local feature of the signal at each point ω_0. Secondly, the steerability theoretically gives access to the orientation and signed-intensity of these local features. Finally, from the computational point of view, the calculation of a directional correlation at each analysis scale is an extremely demanding task. The relation of steerability is essential to reduce the complexity of calculation of the wavelet coefficients when local orientations are considered (Wiaux et al. 2006b).

2.2 Statistical anisotropy or non-Gaussianity?

As already discussed in the introduction, under the cosmological principle assumption and in the framework of the standard inflationary scenario, the CMB signal can be interpreted as a realization of a Gaussian and statistically isotropic random field.

It is not a trivial task to develop an analysis procedure for testing statistical properties with only one realization (because there is only one Universe) of the CMB signal. Typically, the data are contaminated by noise and foreground emissions. Simulations accounting for these peculiarities must be performed to test the compatibility of the data with a given set of assumptions. There are infinite ways of simulating departures from Gaussianity or statistical isotropy. But unless one is interested in the compatibility of the data with a specific alternative model (considering for example a non-standard inflationary scenario, an anisotropic Universe, a non-trivial topology of the Universe, topological defects, etc.), simulations are produced following the concordance model. In that context, any statistical incompatibility of the data with the simulations is to be interpreted as a departure from the whole assumption of Gaussianity and statistical isotropy. Despite that, postulating Gaussianity allows one to interpret a detection as a departure from statistical isotropy, and conversely. Typically, analyses using local estimators on the sphere, for example local power spectra,

can naturally identify preferred directions and probe statistical isotropy, provided that Gaussianity is postulated. On the contrary, analyses using global estimators on the sphere, for example statistical moments computed by averages on the whole sphere, explicitly assume statistical isotropy in order to probe Gaussianity.

In this paper, two analysis procedures are considered. The alignment analysis is recalled, which probes the anomalous alignment of local CMB features toward specific directions. A new signed-intensity analysis is also defined, which probes the anomalously high or low temperature of local CMB features. Because of the local nature of the corresponding anomalies on the celestial sphere, we use these analyses as specific probes of the statistical isotropy of the CMB, while its Gaussianity is postulated.

2.3 Alignment analysis procedure

The alignment of local CMB features toward specific directions on the celestial sphere can be probed with steerable wavelets by combining at each analysis scale a and at each point ω_0 the information on the orientation $D^T(\omega_0, a)$ and on the signed-intensity $I^T(\omega_0, a)$ (the superscript T identifies the CMB temperature field) (Wiaux et al. 2006a; Vielva et al. 2006). Firstly, the great circle is defined which passes by the point ω_0 and admits as a tangent the local direction defined by $D^T(\omega_0, a)$. All directions on that great circle are considered to be seen by the local feature at ω_0 with a weight naturally given as the absolute value of the signed-intensity $|I^T(\omega_0, a)|$ at that point. At scale a and in an arbitrary direction ω, the total weight $TW^T(\omega, a)$ is defined as the sum of the $N_{cros}(\omega)$ weights originating from all pixels $\omega_0^{(c)}$ in the original CMB signal, with $1 \leqslant c \leqslant N_{cros}(\omega)$, for which the great circle defined crosses the direction considered:

$$TW^T(\omega, a) = \frac{1}{A} \sum_{c=1}^{N_{cros}(\omega)} |I^T\left(\omega_0^{(c)}, a\right)|. \qquad (9)$$

The factor $A = L N_{pix}^{-1} \sum_{\omega_0 \notin M_a} |I^T(\omega_0, a)|$ simply stands for the normalization of the total weights. It takes into account the total number of pixels on the sphere N_{pix} and the mean number L of pixels on each great circle in the pixelization considered. It also accounts for the presence of an exclusion mask M_a containing the pixels to be excluded from the analysis at each scale a. As discussed in the next section, our analyses are performed on HEALPix pixelizations[1] (Górski et al. 2005). In this scheme, at a given resolution N_{side}, the number of pixels on each great circle is constant and reads $L = 4N_{side} - 1$. These total weights constitute a new signal on the celestial sphere. Notice that the procedure obviously assigns identical total weights to opposite directions, as any great circle on the sphere always contains a direction and its opposite direction on the same axis. In other words, the total weights signal is even under parity in the three-dimensional

Cartesian coordinate system $(o, o\hat{x}, o\hat{y}, o\hat{z})$ centered on the sphere. The analysis of this signal can be restricted to the directions ω in one arbitrary hemisphere of reference. In
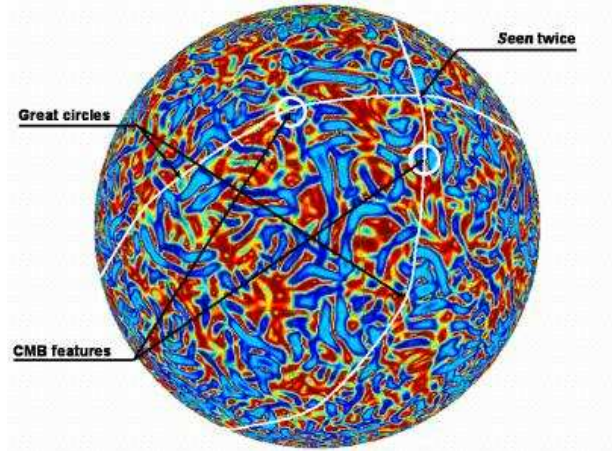

Figure 1. Alignment analysis procedure: example of signed-intensity distribution on the celestial sphere. At each point ω_0, the great circle is defined which passes by ω_0 and admits as a tangent the direction of the local feature at that point, defined by $D^T(\omega_0, a)$. All directions on that great circle are considered to be seen by the local CMB feature at ω_0, with a weight naturally given as the absolute value of the signed-intensity $|I^T(\omega_0, a)|$ at that point. At each analysis scale a, the total weight $TW^T(\omega, a)$ in each direction ω is defined as the sum of the weights originating from all pixels for which the great circle defined crosses the direction considered. The total weights signal on the celestial sphere is even under parity. In an arbitrary hemisphere of reference, the biggest total weights identify the directions toward which the CMB features are predominantly aligned, while the lowest total weights identify the directions predominantly avoided by the CMB features.

that hemisphere, the biggest total weights identify the directions toward which the CMB features are predominantly aligned, while the lowest total weights identify the directions predominantly avoided by the CMB features. An illustration of the procedure described is given in Figure 1.

The signal of total weights is analyzed by comparison with the values obtained from simulations[2] at the same scale a and in the same direction ω. Ten thousand simulations were produced for the analysis. At each point ω of the pixelization considered, the cumulative probability that the simulations exhibit a lower value than the simulation with the ith lowest value is $(i - 0.5) \times 10^{-2}\%$. The cumulative probability that the simulations exhibit a lower value than the data is computed by linear interpolation between the cumulative probabilities assigned to the two neighbour simulations with values directly surrounding the value of the data. A value of the data lower than all simulation values is assigned a cumulative probability of 0.005%, while a value of the data higher than all simulation values is assigned a cumulative probability of 99.995%. Let $\mu_{TW}^T(\omega, a)$ be the median total weight value predicted by the Gaussian and statistically isotropic simulations. Directions with a to-

---

[1] http://healpix.jpl.nasa.gov/

[2] Notice that analyzed maps are intrinsically anisotropic. This is due to the statistical anisotropy of the noise and to the presence of a mask that cuts the brightest foreground emissions (see Subsection 3.1). The statistical distribution of local quantities must therefore be computed independently at each pixel, through the means of simulations.

tal weight higher than the median value of the simulations, $TW^T(\omega, a) \geqslant \mu_{TW}^T(\omega, a)$, are said to bear a positive total weight. Directions with a total weight lower than the median value of the simulations, $TW^T(\omega, a) \leqslant \mu_{TW}^T(\omega, a)$, are said to bear a negative total weight. For positive total weights, a direction ω is defined to be anomalous at a percentage p if the corresponding cumulative probability that the simulations exhibit a lower value than the data is higher or equal to p. For negative total weights, a direction ω is defined to be anomalous at a percentage p if the corresponding cumulative probability that the simulations exhibit a lower value than the data is lower or equal to $1 - p$. In the following, the precise threshold $p = 99.865\%$ is considered because it formally corresponds to the $+3\sigma$ and -3σ values in a Gaussian distribution, for positive and negative total weights respectively. In other words, a direction ω with a positive total weight value of the data higher or equal to the 9987th lowest simulation value (*i.e.* at maximum 14 simulations exhibit a value higher or equal) is considered to be anomalous at 99.865%. A direction ω with a negative total weight value of the data lower or equal to the 14th lowest simulation value (*i.e.* at maximum 14 simulations exhibit a value lower or equal) is also considered to be anomalous at 99.865%.

The global significance level for an alignment detection is estimated as the percentage of simulations with a number of anomalous directions higher or equal to the number of anomalous directions in the data. The lower the significance level, the stronger the detection. Notice that instrumental noise or spurious emissions might produce isolated anomalous directions, corresponding to isolated anomalous pixels. The estimation of the global significance level corrects for that effect in the total count, by weighting isolated anomalous pixels with a low clustering index, and weighting anomalous pixels surrounded by other anomalous pixels, *i.e.* clustered anomalous directions, with a high clustering index. This clustering index is calculated as the fraction of anomalous pixels in a disk with a diameter equal to the angular size of the wavelet at scale a.

2.4   Signed-intensity analysis procedure

Alternatively, the statistical isotropy of the CMB signal can be probed with steerable wavelets by simply considering at each analysis scale a the signed-intensity $I^T(\omega_0, a)$ of the local CMB features at each point ω_0 on the celestial sphere.

The signed-intensity signal (see Figure 1) is also analyzed by comparison with the values obtained from simulations at the same scale a and in the same direction ω. At each point ω of the pixelization considered, the cumulative probability that the simulations exhibit a lower value than the data is computed through the exact same procedure as for the alignment analysis, by linear interpolation from the values of the ten thousand simulations. The median signed-intensity value predicted by the Gaussian and statistically isotropic simulations is zero in each direction as the CMB temperature fluctuations are defined with zero statistical mean. Positive signed-intensities, $I^T(\omega_0, a) \geqslant 0$, therefore indicate directions with a temperature higher than the median value of the simulations. Negative signed-intensities, $I^T(\omega_0, a) \leqslant 0$, indicate directions with a temperature lower than the median value of the simulations. Again, for positive signed-intensities, a direction ω is defined to be anomalous

at a percentage p if the corresponding cumulative probability that the simulations exhibit a lower value than the data is higher or equal to p. For negative signed-intensities, a direction ω is defined to be anomalous at a percentage p if the corresponding cumulative probability that the simulations exhibit a lower value than the data is lower or equal to $1 - p$. We still take $p = 99.865\%$, corresponding to the $+3\sigma$ and -3σ values in a Gaussian distribution, for positive and negative signed-intensities respectively.

The global significance level for a signed-intensity detection is also estimated as the percentage of simulations with a number of anomalous directions higher or equal to the number of anomalous directions in the data, still weighting each anomalous pixel by its clustering index.

3   WMAP ANALYSES

In this section, we firstly discuss the WMAP three-year data and simulations used for our analyses. Secondly, we present the results of the alignment and signed-intensity analyses.

3.1   Data and simulations

Firstly, we consider the data. We have analyzed the three-year WMAP data after correction for foreground emissions contamination by a template fitting technique (Spergel et al. 2007). This procedure provides eight cleaned maps at various frequencies for the corresponding WMAP radiometers: Q1 and Q2 at 41 GHz, V1 and V2 at 61 GHz, and W1, W2, W3, and W4 at 94 GHz. These maps are available from the NASA LAMBDA archive[3]. After foreground emissions removal, these maps are masked with the Kp0 mask (Spergel et al. 2007) that cuts the regions ($\approx 20\%$ of the sky) with the brightest galaxy emission and the positions ($\approx 5\%$ of the sky) where the brightest known point sources are located, assigning zero values to the corresponding pixels. It is assumed that the CMB is convolved with an instrumental beam that is well described by an isotropic window function and that the instrumental noise is to first order Gaussian, statistically anisotropic, and uncorrelated. Maps with better signal-to-noise ratio can be obtained, by an optimal combination of the eight cleaned maps obtained after foreground emissions removal and masking. At each pixel, this combination is obtained by weighting each map by the corresponding inverse noise variance to produce the so-called three-year WMAP co-added CMB map (Hinshaw et al. 2007), denoted here the WCM123 map. For the sake of the analysis, this map is considered to contain only CMB and instrumental noise. The residual foreground emissions are considered to be negligible.

In addition to the WCM123 map, other maps are produced for different analysis purposes. Three maps are built to optimize signal-to-noise ratio at each frequency by combining the foreground cleaned and masked maps of the corresponding radiometers: the WCM-Q, WCM-V, and WCM-W. These frequency maps obviously contain CMB and instrumental noise, as well as residual foreground emissions which are precisely not neglected by principle. They

---

[3] http://lambda.gsfc.nasa.gov/

are actually used to test whether detected anomalies are due to residual foreground emissions, which are frequency-dependent. Three other maps are also produced to remove in depth both CMB and residual foreground emissions at each frequency by subtracting the foreground cleaned and masked maps of the corresponding radiometers: Q1 - Q2 defines the WCM-nQ map, V1 - V2 defines the WCM-nV maps, and W1 - W2 + W3 - W4 defines the WCM-nW map. Despite negligible CMB and foreground emissions residuals at small angular sizes (well below $1°$) due to the different beam window functions of the radiometers at each frequency, these difference maps essentially contain instrumental noise. They are used to test whether detected anomalies are due to any effect associated with instrumental noise. A last map is produced to remove in depth only CMB by subtracting the foreground cleaned and masked maps at different frequencies, defining the WCM-nWVQ map as W1 + W2 + W3 + W4 -V1 - V2 - Q1 - Q2. Despite negligible CMB residuals at small angular sizes (well below $1°$) again due to the different beam window functions of the radiometers at each frequency, this difference map essentially contains instrumental noise and residual foreground emissions. It can be used as an additional test of the impact of instrumental noise and residual foreground emissions on detected anomalies.

In order to minimize any contamination coming from errors on the cosmological dipole subtraction, the dipole outside the mask is removed from each analyzed map (Komatsu et al. 2003).

All these maps are initially produced in HEALPix pixelization at the resolution $N_{side} = 512$, corresponding to maps with several million equal-area pixels with a spatial resolution of $6.9'$. For the sake of our analysis, which is applied at wavelet scales corresponding to angular sizes between $5°$ and $30°$, they are downgraded to the resolution $N_{side} = 32$. This provides maps with $N_{pix} = 12288$ equal-area pixels with a spatial resolution of $1.8°$.

Secondly, we consider the simulations. Each of the simulations used to compare the results of the analysis of the data to what is expected from the concordance model was produced as follows. The spherical harmonics coefficients of a Gaussian and statistically isotropic CMB realization are obtained from the angular power spectrum determined by the cosmological parameters of the three-year WMAP best-fit model (Spergel et al. 2007) with CAMB (Code for Anistropies in the Microwave Background[4]). The observation at each of the eight WMAP radiometers considered is simulated by convolving that signal in harmonic space with the corresponding isotropic window function. Each map is then transformed to pixel space at the resolution $N_{side} = 512$, and a Gaussian and statistically anisotropic noise realization is added with the proper dispersion per pixel. This provides simulations of the CMB signal, as seen by the radiometers at the different WMAP frequencies considered. The same prescriptions as those described above for the data are then applied to produce one simulated coadded map (WCM123), three simulated frequency maps (WCM-Q, WCM-V, and WCM-W), and three simulated difference maps (WCM-nQ, WCM-nV, WCM-nW, and WCM-
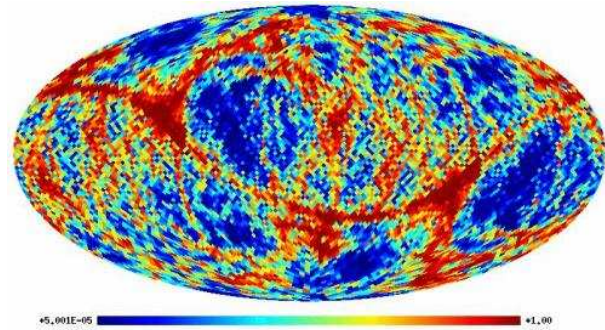
Figure 2. Alignment analysis: cumulative probabilities map in Mollweide projection for the total weights $TW^T(\omega, a_3)$ computed from the WCM123 map, at wavelet scale a_3 corresponding to $8.3°$ of angular size. The pattern observed presents several great circles of high positive (in red) or negative (in blue) total weights on the celestial sphere, respectively corresponding to directions with a total weight value well higher, or lower, than the median value of the simulations.

nWVQ). These simulations are then also downgraded at the resolution $N_{side} = 32$ for our analysis.

Ten thousand simulations of the WCM123 map were produced for the main analysis. In order to reduce the corresponding computation time, only one thousand simulations were considered for the frequency maps and difference maps used to analyze the origin of a possible detection in terms of instrumental noise or foreground emissions. This is by far enough since no precise significance level is established from the analysis of these maps. Only the general patterns of possible detections are studied in comparison with the patterns observed from the analysis of the WCM123 map.

Finally, in valid pixels close to masked regions, the result of the directional correlation of a signal with steerable wavelets at a given scale of analysis is inevitably affected by the zero values of the Kp0 mask. On each of the maps presented above, and obviously both for the data and simulations, an exclusion mask M_a is therefore defined at each wavelet scale a in order to exclude the affected pixels from the analysis (Vielva et al. 2004).

3.2 Alignment analysis

We have performed the alignment analysis on the WCM123 map with the 2GD at twelve wavelet scales a_i ($1 \leqslant i \leqslant 12$) corresponding to angular sizes between $5°$ and $30°$. The wavelet half-widths θ_{hw} corresponding to the scales a_1 to a_{12} respectively read in arcminutes as: $\{150', 200', 250', 300', 350', 400', 450', 500', 550', 600', 750', 900'\}$. The map of the cumulative probabilities that the simulations exhibit a lower value than the data for the total weights $TW^T(\omega, a_3)$ at wavelet scale a_3, corresponding to $8.3°$ of angular size, is presented in Figure 2. One can easily acknowledge that the pattern of direction preferences presents several great circles on the celestial sphere. At that scale, an anomaly in the alignment of the local CMB features is actually observed, which is detailed in the following.

Let us recall that the total weights signal is even under parity, and its analysis can be restricted to one hemisphere of reference. Considering for instance the northern galactic hemisphere, 67 directions anomalous at 99.865% are iden-
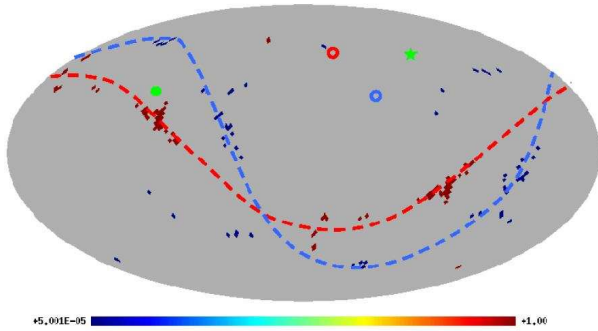
Figure 3. Alignment analysis: thresholded cumulative probabilities map in Mollweide projection for the total weights $TW^T(\omega, a_3)$ computed from the WCM123 map, at wavelet scale a_3 corresponding to $8.3°$ of angular size. The total weights signal is even under parity, and its analysis can be restricted to one hemisphere of reference. Considering for instance the northern galactic hemisphere, 67 directions anomalous at 99.865% are retained. The global significance level of detection is 0.85%. The directions with positive total weights (in red) define a first mean preferred plane (red dashed line) in the sky, with a normal axis (red circle) close to the CMB dipole axis (green asterisk). In this plane, a prominent cluster of directions identifies a mean preferred axis very close to the ecliptic poles axis (green disk). The directions with negative total weights (in blue) define a second mean preferred plane (blue dashed line) with a normal axis (blue circle) again close to the CMB dipole axis.
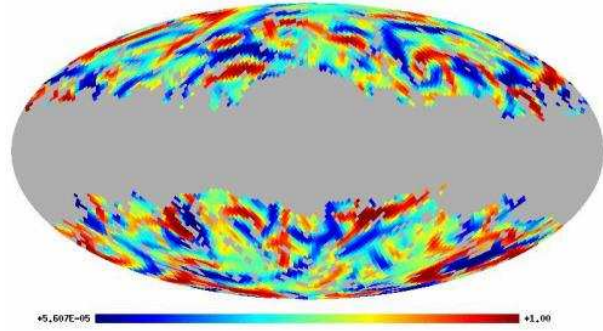

Figure 4. Signed-intensity analysis: cumulative probabilities map in Mollweide projection for the signed-intensities $I^T(\omega, a_3)$ computed for the WCM123 map, at wavelet scale a_3 corresponding to $8.3°$ of angular size. The pattern observed presents several well located spots of high positive (in red) or negative (in blue) signed-intensities on the celestial sphere, respectively corresponding to directions with a temperature value well higher, or lower, than the median value of the simulations.

tified at wavelet scale a_3. These anomalous directions are represented in Figure 3. The global significance level of detection is 0.85%. Among these directions, 39 exhibit positive total weights, corresponding to directions with a total weight value well higher than the median value of the simulations. They are essentially aligned along a great circle, which defines a first mean preferred plane in the sky, toward which local CMB features are anomalously aligned. The normal axis to this plane, whose northern end is identified by $(\theta, \varphi) = (39°, 337°)$ in galactic co-latitude θ and longitude φ, lies close to the CMB dipole axis, with northern end at $(\theta, \varphi) = (42°, 264°)$, and close to the axis of evil, with northern end at $(\theta, \varphi) = (30°, 260°)$. In this plane, a prominent cluster of anomalous directions toward which local features are anomalously aligned identifies a mean preferred axis whose northern end lies at $(\theta, \varphi) = (73°, 91°)$, very close to the ecliptic poles axis, with northern end at $(\theta, \varphi) = (60°, 96°)$. The 28 remaining anomalies exhibit negative total weights, corresponding to directions with a total weight value well lower than the median value of the simulations. They are also essentially aligned along a great circle, which defines a second mean preferred plane in the sky, of directions anomalously avoided by the local CMB features. The normal axis to this plane, whose northern end is identified by $(\theta, \varphi) = (59°, 309°)$, lies also close to the CMB dipole axis and to the axis of evil. The whole structure of the present detection hence provides further insight into the anomaly recently observed (Wiaux et al. 2006a) on the one-year WMAP co-added CMB map (Bennett et al. 2003b). It again synthesizes the previously reported statistical anisotropy results by highlighting both the ecliptic poles axis and the CMB dipole axis as preferred axes in the sky.

The detection is confirmed at wavelet scale a_4, corre-

sponding to $10°$ of angular size. At this scale, in one hemisphere of reference, 62 directions anomalous at 99.865% are identified. The global significance level of detection is 1.28%. Among these directions, 38 exhibit positive total weights, and the 24 remaining exhibit negative total weights. They define the same pattern of anomaly as the one observed at wavelet scale a_3.

3.3 Signed-intensity analysis

We have performed the signed-intensity analysis on the WCM123 map with the 2GD at the same scales as for the alignment analysis, corresponding to angular sizes between $5°$ and $30°$. The map of the cumulative probabilities that the simulations exhibit a lower value than the data for the signed-intensities $I^T(\omega_0, a_3)$ at wavelet scale a_3 corresponding to $8.3°$ of angular size, is presented in Figure 4. The pattern observed is actually similar to the one obtained through the axisymmetric Mexican hat wavelet analysis (Vielva et al. 2004, Figure 12), presenting several well located spots of high positive or negative signed-intensities on the celestial sphere. Beyond that similarity, at that scale, an anomaly in the signed-intensity of the local CMB features is observed, which is detailed in the following.

Considering here the whole celestial sphere and of course not only one hemisphere, 39 directions anomalous at 99.865% are identified at wavelet scale a_3. These anomalous directions are represented in Figure 5. The global significance level of detection is 1.39%. Among these directions, 24 exhibit negative signed-intensities, corresponding to directions with a temperature value well lower than the median value of the simulations. The 15 remaining anomalies exhibit positive signed-intensities, corresponding to directions with a temperature value well higher than the median value of the simulations. The anomalous directions are actually distributed in three clusters in the southern galactic hemisphere, identifying three mean preferred directions in the sky. A first cold spot (*i.e.* of negative signed-intensities) centered at $(\theta, \varphi) = (150°, 209°)$ in galactic co-latitude θ and longitude φ, essentially identifies with the known cold spot centered at $(\theta, \varphi) = (147°, 209°)$ (Vielva et al. 2004).
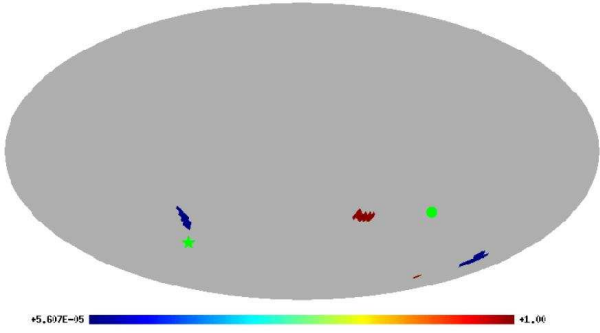
Figure 5. Signed-intensity analysis: thresholded cumulative probabilities map in Mollweide projection for the signed-intensities $I^T(\omega, a_3)$ computed for the WCM123 map, at wavelet scale a_3 corresponding to $8.3°$ of angular size. On the whole celestial sphere, 39 directions anomalous at 99.865% are retained. The global significance level of detection is 1.39%. The anomalous directions are distributed in three clusters in the southern galactic hemisphere, identifying three mean preferred directions in the sky. A first cold spot (in blue) identifies with a known cold spot (Vielva et al. 2004). A second cold spot (in blue) lies very close to the southern end of the CMB dipole axis (green asterisk). The third spot is a hot spot (in red) close to the southern end of the ecliptic poles axis (green disk).

A second cold spot is centered at $(\theta, \varphi) = (129°, 80°)$, very close to the southern end of the CMB dipole axis at $(\theta, \varphi) = (138°, 84°)$. The third spot is a hot spot (*i.e.* of positive signed-intensities) centered at $(\theta, \varphi) = (124°, 321°)$, close to the southern end of the ecliptic poles axis, at $(\theta, \varphi) = (120°, 276°)$. In conclusion, this detection again synthesizes previously reported statistical anisotropy results. Indeed, it confirms the North-South asymmetry, to which the cold spot centered at $(\theta, \varphi) = (147°, 209°)$ was originally related. Moreover, two other spots are identified in the southern galactic hemisphere which contribute to the North-South asymmetry, and with specific positions once more close to both the ecliptic poles axis and the CMB dipole axis.

The detection is confirmed at wavelet scales a_4, a_5, and a_6, respectively corresponding to $10°$, $11.7°$, and $13.3°$ of angular sizes. The three spots are explicitly recovered, with global significance levels below 4.90%. In particular at wavelet scale a_4, 42 directions anomalous at 99.865% are identified on the whole celestial sphere, among which 29 exhibit negative signed-intensities, and 13 exhibit positive signed-intensities. The global significance level of detection is 1.97%.

Let us also emphasize the peculiar distribution on the celestial sphere of the three spots detected, which are roughly separated two by two by right angles. They identify the three basis vectors of a coordinate frame with the North pole close to the southern end of the ecliptic poles axis. The hot spot coincides with the North pole, and the cold spots roughly lie in the perpendicular plane, with one of them very close to the southern end of the CMB dipole axis.

3.4 All-scale significance level

An all-scale significance level may be computed, which should account for the fact that twelve wavelet scales have

been probed, hence artificially increasing chances of detection at one or another scale. But it should also account for all the detections observed in both the alignment and the signed-intensity analyses. In the data, the two alignment detections at the wavelet scales a_3 and a_4, and the four signed-intensity detections at the wavelet scales a_3, a_4, a_5, and a_6 are observed at global significance levels roughly lower than 5.00%. In a conservative approach, the all-scale significance level defined is estimated as the percentage of simulations with a global significance level lower or equal to 5.00% for at least two consecutive scales in the alignment analysis, and at least four consecutive scales (not necessarily related with the first two) in the signed-intensity analysis. The corresponding value for this robust all-scale significance level is 1.50%. This actually confirms the best levels of detections observed in the data in terms of global significance levels at individual wavelet scales in each of the two analyses.

4 ANOMALIES ORIGIN

In this section, we firstly establish that the alignment and signed-intensity anomalies detected are only very partially related. Secondly, we consider and discard possible origins of these anomalies in terms of instrumental noise, foreground emissions, and some form of unknown systematics.

4.1 Anomalies relation

The alignment and signed-intensity anomalies both highlight the ecliptic poles axis and the CMB dipole axis as preferred axes in the sky. Moreover, in terms of procedure, the alignment analysis based on the definition (9) of total weights can be interpreted as a variation of the signed-intensity analysis, taking into account the orientation of local CMB features. Consequently, it is natural to raise the question of a possible relation between the corresponding anomalies detected. More precisely, one can verify if the part of the alignment anomaly associated with positive total weights originates, at least partially, in the signed-intensity anomaly. In order to probe this hypothesis, the alignment analysis was repeated on the WCM123 map, in which each of the three spots responsible for the signed-intensity anomaly was in turn excluded from the analysis. In that regard, the pixels corresponding to the spot considered were simply included in the exclusion mask.

When the hot spot close to the ecliptic poles axis is excluded, the number of directions anomalous at 99.865% associated with positive total weights drops, in one hemisphere of reference, from 39 to 28 at wavelet scale a_3, and the corresponding global significance level increases from 0.87% to 2.38%. At wavelet scale a_4, the number of directions anomalous at 99.865% associated with positive total weights drops, again in one hemisphere of reference, from 38 to 18, and the corresponding global significance level increases more drastically from 1.66% to 17.31%. On the contrary, there is no significant impact on the alignment anomaly of neither of the two cold spots responsible for the signed-intensity anomaly. In other words, the hot spot of anomalous signed-intensities is partially, but certainly not totally, responsible for the part of the alignment anomaly associated with positive total weights, while the two cold spots have no significant impact

on it. The observed alignment anomaly associated with positive total weights (see Figure 3) is therefore not due to the alignment of a small number of local CMB features with an anomalous signed-intensity. It is rather due to the alignment of a large number of local CMB features with a non-anomalous signed-intensity. This result is in agreement with a previous analysis showing that the local CMB features aligned toward the directions exhibiting anomalous positive total weights are essentially homogeneously distributed on the celestial sphere (Vielva et al. 2006). In conclusion, the alignment anomaly observed originates only very partially in the signed-intensity anomaly.

4.2   Instrumental noise and foreground emissions

Before claiming a possible cosmological origin of the detections reported, it is essential to look for possible origins in terms of instrumental noise or foreground emissions.

A possible origin in terms of instrumental noise in the WCM123 map is analyzed by reproducing the analyses on the difference maps WCM-nQ, WCM-nV, and WCM-nW, which are essentially noise maps (see Subsection 3.1). In particular, it is known that the WMAP data present a small component of correlated noise at large angular sizes (well above $1°$), which is not taken into account in our simulations. This instrumental noise might be detected through the analysis of these difference maps. Moreover, the pattern of this correlated noise is related to the ecliptic coordinates system through the WMAP scanning strategy. It is therefore a plausible origin of the alignment and signed-intensity anomalies observed. The corresponding maps representing the cumulative probabilities that the simulations exhibit a lower value than the data are presented in Figure 6, both for the total weights $TW^T(\omega, a_3)$ and signed-intensities $I^T(\omega, a_3)$ at wavelet scale a_3. The total weights and signed-intensities patterns revealed do not correspond to those obtained from the WCM123 map on which the anomalies are observed. Instrumental noise can therefore be discarded as a possible origin of the alignment and signed-intensity detections.

A possible origin in terms of residual foreground emissions in the WCM123 map is analyzed by reproducing the analyses on the frequency maps WCM-Q, WCM-V, and WCM-W, which contain essentially CMB, with instrumental noise and residual foreground emissions (see Subsection 3.1). The analyses are also reproduced on the difference map WCM-nWVQ which essentially contains instrumental noise and residual foreground emissions (see Subsection 3.1). The corresponding maps representing the cumulative probabilities that the simulations exhibit a lower value than the data are presented in Figure 7, both for the total weights $TW^T(\omega, a_3)$ and signed-intensities $I^T(\omega, a_3)$ at wavelet scale a_3. The total weights and signed-intensities patterns obtained from the WCM-Q, WCM-V , and WCM-W maps are similar to those obtained from the WCM123 map on which the anomaly is observed. Consequently, the detection is independent of the frequency. As foreground emissions themselves are frequency-dependent, they may be discarded as a possible origin of the alignment and signed-intensity detections reported above. Moreover, the total weights and signed-intensities patterns obtained from the WCM-nWVQ maps do not correspond to those obtained from the WCM123 map. This is an additional evidence

that instrumental noise and foreground emissions can be discarded as possible origins of the alignment and signed-intensity detections.

4.3   Unknown systematics

In the absence of instrumental noise or foreground emissions explanations, the fact that the ecliptic poles axis and the CMB dipole axis are strongly highlighted through our detections as preferred axes in the sky still suggests the possible presence of unknown systematics, more than a cosmological origin of the detections. These directions are indeed local concepts with *a priori* no global cosmological meaning.

The wavelet analysis allowed us to identify the scales, roughly around $10°$ of angular size, at which the anomalies are observed. This represents an important complementary piece of information in the search for their origin. Let us recall in that respect that the size of the mesh of the WMAP scanning pattern defined by the combination of the spin and precession of the satellite is of the order of several degrees (Bennett et al. 2003c). Moreover, the WMAP scanning strategy is also obviously connected to the ecliptic coordinates system. Unknown systematics related to the WMAP scanning strategy are therefore a plausible source of the detected anomaly.

In that vein, it was recently suggested that North-South asymmetries can in principle be explained by a bad calibration of the CMB dipole (Freeman et al. 2006). More generally it was also suggested that a modulation $T(\omega) \times [1 + f(\omega)]$ of the CMB temperature field $T(\omega)$ with a modulation function $f(\omega)$, potentially coming from systematic effects, could in turn explain North-South asymmetries and low multipoles alignment (Helling et al. 2006; Gordon 2007). A dipolar modulation function, *i.e.* containing only the multipole $l = 1$, which provides the best fit between the three-year WMAP data and the concordance model was proposed (Eriksen et al. 2007). A best-fit dipolar-quadrupolar modulation function, *i.e.* containing the multipoles $l = 1$ and $l = 2$, was also proposed (Spergel et al. 2007, see arXiv:astro-ph/0603449v1). A possible origin of our anomalies in terms of a dipolar or dipolar-quadrupolar modulation is probed by reproducing the alignment and signed-intensity analyses on the WCM123 map correspondingly corrected[5].

Firstly, the results induced by the dipolar correction are as follows. The alignment anomaly is preserved at the wavelet scales a_3 and a_4. The general pattern of anomalous directions still highlights the same two mean preferred planes and the same mean preferred axis in the sky. The global significance level of detection is not significantly modified at neither of the two scales. The signed-intensity

---

[5] Let us remark that the modulations used were not primarily computed for the WCM123 itself. The dipolar modulation considered was produced by (Eriksen et al. 2007) for the Internal Linear Combination (ILC) map defined in (Hinshaw et al. 2007), at HEALPix resolution $N_{side} = 16$. The dipolar-quadrupolar modulation considered was produced by (Spergel et al. 2007, see arXiv:astro-ph/0603449v1) for the frequency map WCM-V with Kp2 mask at HEALPix resolution $N_{side} = 8$. However, the best-fit modulations were shown not to be sensitive to the three-year WMAP data set and sky cut. They are therefore also adequate for correction of the WCM123 map.
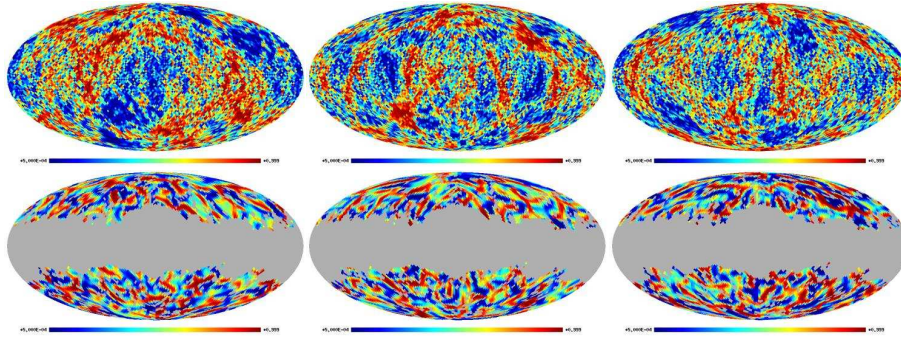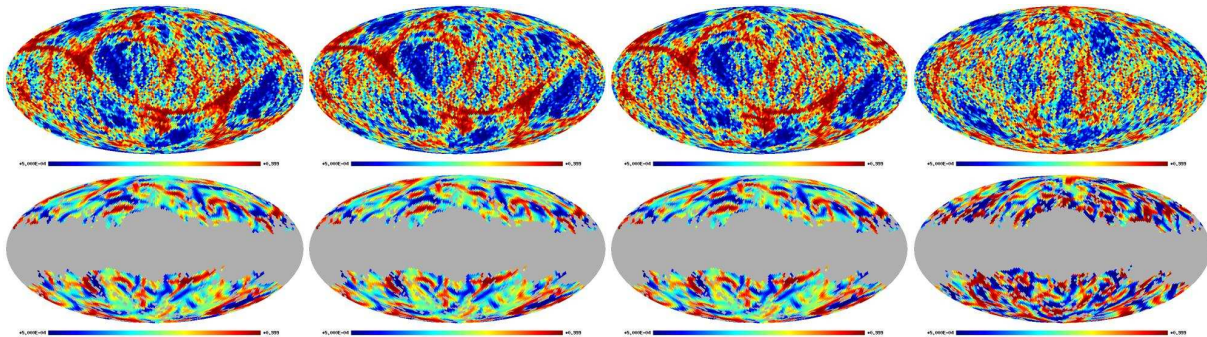
Figure 6. Alignment and signed-intensity analyses: cumulative probabilities maps in Mollweide projection for the total weights $TW^T(\omega, a_3)$ (top panel) and signed-intensities $I^T(\omega, a_3)$ (bottom panel) at wavelet scale a_3, resulting from the difference maps WCM-nQ (left column), WCM-nV (center column), and WCM-nW (right column). The total weights and signed-intensities patterns do not correspond to those obtained from the WCM123 map. Instrumental noise can be therefore be discarded as a possible origin of the alignment and signed-intensity detections.

Figure 7. Alignment and signed-intensity analyses: cumulative probabilities maps in Mollweide projection for the total weights $TW^T(\omega, a_3)$ (top panel) and signed-intensities $I^T(\omega, a_3)$ (bottom panel) at wavelet scale a_3, resulting from the frequency maps WCM-Q (extreme left column), WCM-V (center-left column), WCM-W (center-right column), and the difference map WCM-nWVQ (extreme right column). The total weights and signed-intensities patterns obtained from the WCM-Q, WCM-V, and WCM-W maps are similar to those obtained from the WCM123 map. Foreground emissions can therefore be discarded as a possible origin of the alignment and signed-intensity detections. The total weights and signed-intensities patterns obtained from the WCM-nWVQ map do not correspond to those obtained from the WCM123 map. This is an additional evidence that instrumental noise and foreground emissions can be discarded as possible origins of the alignment and signed-intensity detections.

anomaly is decreased at all the wavelet scales a_3, a_4, a_5, and a_6, even though the general pattern of anomalous directions still highlights the same three spots in the southern galactic hemisphere. The axis of the dipolar modulation has its southern end at $(\theta, \varphi) = (117°, 225°)$, close to the cold spot centered at $(\theta, \varphi) = (150°, 209°)$. The correction consequently reduces the number of anomalous pixels which define that spot, thereby reducing its impact on the anomaly (Eriksen et al. 2007). The other two spots are essentially left unchanged as they lie in the perpendicular plane, where the dipolar modulation is negligible. The global significance level of detection is increased at all scales. Typically, at the main wavelet scale of detection a_3, the global significance level rises from 1.39% to 4.39%.

Secondly, the results induced by the dipolar-quadrupolar correction are as follows. The alignment anomaly is enhanced at the wavelet scales a_3 and a_4. The general pattern of anomalous directions still highlights the same two mean preferred planes and the same mean preferred axis in the sky. The global significance level of detection is significantly decreased at both scales. Typically, at the main wavelet scale of detection a_3, the global signif-

icance level drops from 0.85% to 0.19%. The distribution of the signed-intensity anomalies on the celestial sphere is affected at all the wavelet scales a_3, a_4, a_5, and a_6, even though the general pattern of anomalous directions still highlights the same three spots in the southern galactic hemisphere. The correction pattern is such that it still reduces the number of anomalous pixels which define the cold spot centered at $(\theta, \varphi) = (150°, 209°)$, while enhancing the number of pixels defining the hot spot. The second cold spot is essentially left unchanged. The global significance level of detection is not significantly modified at none of the scales.

Consequently, the modulations considered clearly fail to explain the alignment and signed-intensity anomalies. Moreover the impact of the correction is extremely sensitive to the arbitrary choice of the dipolar or dipolar-quadrupolar nature of the modulation. The existence of such a modulation, and its precise pattern, still need to be physically verified in terms of specific systematic effects before full credit may be given to the modifications induced.

In conclusion, neither instrumental noise nor foreground emissions seem to explain the alignment and signed-intensity

anomalies reported. And first attempts to consider unknown systematics, potentially related to the WMAP scanning strategy, also failed to explain our detections. Consequently, a cosmological origin imprinted in the CMB can actually not be discarded. In that regard, as already emphasized (Wiaux et al. 2006a), let us notice that the average wavelet scale at which our detections are made, around $10°$ of angular size on the celestial sphere, is compatible with the size of primary CMB anisotropies due to topological defects such as texture fields (Turok & Spergel 1990) or secondary anisotropies due to the Rees-Sciama effect (Martínez-González & Sanz 1990).

5 CONCLUSION

A significant statistical anisotropy was detected on the three-year WMAP data of the CMB, through a decomposition of the signal with steerable wavelets on the sphere.

Firstly, the alignment analysis of local CMB features performed on the three-year WMAP data provides further insight on results obtained from the one-year WMAP data analysis (Wiaux et al. 2006a). At a wavelet scale corresponding to an angular size of $8.3°$ on the celestial sphere, a peculiar pattern of directions anomalous at 99.865% ($\pm 3\sigma$ Gaussian) is detected, with a global significance level of 0.85%. Two mean preferred planes are identified in the sky, whose normal axes lie close to the CMB dipole axis. The first plane is defined by the directions toward which the local CMB features are anomalously aligned. In this plane, a prominent cluster of anomalous directions defines a mean preferred axis very close to the ecliptic poles axis. The second plane is defined by the directions anomalously avoided by the local CMB features.

Secondly, the signed-intensity analysis of local CMB features performed on the three-year WMAP data allows one to detect, at the same wavelet scale, another specific pattern of directions anomalous at 99.865%, with a global significance level of 1.39%. It points out three clusters of anomalously high or low temperature in the southern galactic hemisphere, thereby defining three mean preferred directions in the sky. A first one essentially identifies with a known cold spot (Vielva et al. 2004). A second one is a cold spot very close to the southern end of the CMB dipole axis. The third one is a hot spot close to the southern end of the ecliptic poles axis.

Both detections are confirmed at neighbour wavelet scales corresponding to slightly larger angular sizes on the celestial sphere. A robust all-scale significance level is also estimated which accounts at once for the twelve wavelet scales probed and for the detections observed at various scales in both the alignment and signed-intensity analyses. Its value is of 1.50%, which confirms the best levels of detections observed in the data in terms of global significance levels at individual wavelet scales in each of the two analyses.

Finally, we analyzed a possible relation between both anomalies, and probed their possible origins. The hot spot of the signed-intensity anomaly is partially, but certainly not totally, responsible for the part of the alignment anomaly associated with the directions toward which the local CMB features are anomalously aligned. Hence, the alignment and signed-intensity anomalies observed are only very partially

related. Further analyses on frequency maps and differences of frequency maps strongly reject instrumental noise and foreground emissions as possible origins of our detections. Nevertheless, the fact that the detection once more highlights the ecliptic poles axis and the CMB dipole axis as preferred axes in the sky still calls for an explanation of the origin of the anomalies in terms of systematics, possibly related to the WMAP scanning strategy. We performed a simple test in that context, certainly not exhaustive though, following recent suggestions that unknown systematics might induce a modulation of the CMB temperature field. But correcting the three-year WMAP data for the proposed dipolar or dipolar-quadrupolar modulations fails to explain the detected anomalies.

A cosmological origin, that is, a global violation of the isotropy of the Universe inducing an intrinsic statistical anisotropy of the CMB, therefore still remains a plausible explanation of the detected alignment and signed-intensity anomalies.

REFERENCES

Abramo L.R., Bernui A., Ferreira I.S., Villela T., Wuensche C.A., 2006, Phys. Rev. D, 74, 063506

Bennett C.L. et al., 2003a, ApJS, 148, 1

Bennett C.L. et al., 2003b, ApJS, 148, 97

Bennett C.L. et al., 2003c, ApJS, 583, 1

Bernui A., Villela T., Wuensche C.A., Leonardi R., Ferreira I., 2006, A&A, 454, 409

Bernui A., Mota B., Rebouças M.J., Tavakol R., 2007, A&A, 464, 479

Bielewicz P., Eriksen H.K., Banday A.J., Górski K.M., Lilje P.B., 2005, ApJ, 635, 750

Bridges M., McEwen J.D., Lasenby A.N., Hobson M.P., 2006, preprint (arXiv:astro-ph/0605325v1)

Cayón L., Jin J., Treaster A., 2005, MNRAS, 362, 826

Copi C.J., Huterer D., Starkman G.D., 2004, Phys. Rev. D, 70, 043515

Cruz M., Martínez-González E., Vielva P., Cayón L., 2005, MNRAS, 356, 29

Cruz M., Tucci M., Martínez-González E., Vielva P., 2006, MNRAS, 369, 57

Cruz M., Cayón L., Martínez-González E., Vielva P., Jin J., 2007, ApJ, 655, 11

de Oliveira-Costa A., Tegmark M., Zaldarriaga M., Hamilton A., 2004, Phys. Rev. D, 69, 063516

Donoghue E.P., Donoghue J.F., 2005, Phys. Rev. D, 71, 043002

Eriksen H.K., Hansen F.K., Banday A.J., Górski K.M., Lilje P.B., 2004a, ApJ, 605, 14

Eriksen H.K., Novikov D.I., Lilje P.B., Banday A.J., Górski K.M., 2004b, ApJ, 612, 64

Eriksen H.K., Banday A.J., Górski K.M., Lilje P.B., 2005, ApJ, 622, 58

Eriksen H.K., Banday A.J., Górski K.M., Hansen F.K., Lilje P.B., 2007, ApJ, 660, L81

Freeman P.E., Genovese C.R., Miller C.J., Nichol R.C., Wasserman L., 2006, ApJ, 638, 1

Gordon C., 2007, ApJ, 656, 636

Górski K.M., Hivon E., Banday A.J., Wandelt B.D., Hansen F.K., Reinecke M., Bartelmann M., 2005, ApJ, 622, 759

Hajian A., Souradeep T., 2003, ApJ, 597, L5

Hajian A., Souradeep T., Cornish N., 2005a, ApJ, 618, L63

Hajian A., Souradeep T., 2005b, preprint (astro-ph/0501001)

Hansen F.K., Cabella P., Marinucci D., Vittorio N., 2004a, ApJ, 607, L67

Hansen F.K., Banday A. J., Górski K.M., 2004b, MNRAS, 354, 641

Helling R.C., Schupp P., Tesileanu T., 2006, Phys. Rev. D, 70, 063004

Hinshaw G. et al., 2007, ApJS, 170, 288

Jaffe T.R., Banday A.J., Eriksen H.K., Górski K.M., Hansen F.K., 2006a, ApJ, 629, L1

Jaffe T.R., Hervik S., Banday A.J., Górski K.M., 2006b, ApJ, 644, 701

Jaffe T.R., Banday A.J., Eriksen H.K., Górski K.M., Hansen F.K., 2006c, preprint (arXiv:astro-ph/0606046v1)

Katz G., Weeks J., 2004, Phys. Rev. D, 70, 063527

Komatsu E. et al., 2003, ApJS, 148, 119

Land K., Magueijo J., 2005a, MNRAS, 357, 994

Land K., Magueijo J., 2005b, Phys. Rev. Lett., 95, 071301

Land K., Magueijo J., 2006, MNRAS, in press (arXiv:astro-ph/0611518v2)

Martínez-González E., Sanz J.L., 1990, MNRAS, 247, 473

McEwen J.D., Hobson M.P., Lasenby A.N., Mortlock D.J., 2005, MNRAS, 259, 1583

McEwen J.D., Hobson M.P., Lasenby A.N., Mortlock D.J., 2006, MNRAS, 371, 50

McEwen J.D., Wiaux Y., Hobson M.P., Vandergheynst P., Lasenby A.N., 2007, preprint (arXiv:0704.0626v1 [astro-ph])

Mukherjee P., Wang Y., 2004, ApJ, 613, 51

Park C.-G., 2004, MNRAS, 349, 313

Schwarz D.J., Starkman G.D., Huterer D., Copi C.J., 2004, Phys. Rev. Lett., 93, 221301

Spergel D.N. et al., 2003, ApJS, 148, 175

Spergel D.N. et al., 2007, ApJS, 170, 377

Turok N., Spergel D.N., 1990, Phys. Rev. Lett. 64, 2736

Vielva P., Martínez-González E., Barreiro R.B., Sanz J.L., Cayón L., 2004, ApJ, 609, 22

Vielva P., Wiaux Y., Martínez-González E., Vandergheynst P., 2006, New Astron. Rev., 50, 880

Wiaux Y., Jacques L., Vandergheynst P., 2005, ApJ, 632, 5

Wiaux Y., Vielva P., Martínez-González E., Vandergheynst P., 2006a, Phys. Rev. Lett., 96, 151303

Wiaux Y., Jacques L., Vielva P., Vandergheynst P., 2006b, ApJ, 652, 820